A model for acoustic vaporization dynamics of a bubble/droplet system encapsulated within a hyperelastic shell

Thomas Lacour, Matthieu Guédra, Tony Valier-Brasier, François Coulouvrat

A model for acoustic vaporization dynamics of a bubble/droplet system encapsulated within a hyperelastic shell

Thomas Lacour, Matthieu Guédra, Tony Valier-Brasier, and François Coulouvrat

Citation: The Journal of the Acoustical Society of America **143**, 23 (2018); doi: 10.1121/1.5019467
View online: https://doi.org/10.1121/1.5019467
View Table of Contents: https://asa.scitation.org/toc/jas/143/1
Published by the Acoustical Society of America

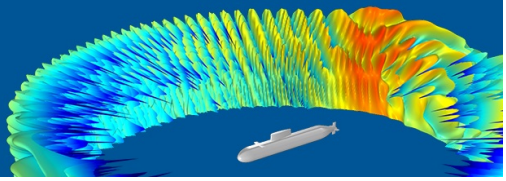

A model for acoustic vaporization dynamics of a bubble/droplet system encapsulated within a hyperelastic shell

Thomas Lacour,[a] Matthieu Guédra, Tony Valier-Brasier, and François Coulouvrat
Sorbonne Université, Centre National de la Recherche Scientifique, UMR 7190, Institut Jean Le Rond ∂'Alembert, F-75005 Paris, France

(Received 6 June 2017; revised 8 December 2017; accepted 10 December 2017; published online 5 January 2018)

Nanodroplets have great, promising medical applications such as contrast imaging, embolotherapy, or targeted drug delivery. Their functions can be mechanically activated by means of focused ultrasound inducing a phase change of the inner liquid known as the acoustic droplet vaporization (ADV) process. In this context, a four-phases (vapor + liquid + shell + surrounding environment) model of ADV is proposed. Attention is especially devoted to the mechanical properties of the encapsulating shell, incorporating the well-known strain-softening behavior of Mooney-Rivlin material adapted to very large deformations of soft, nearly incompressible materials. Various responses to ultrasound excitation are illustrated, depending on linear and nonlinear mechanical shell properties and acoustical excitation parameters. Different classes of ADV outcomes are exhibited, and a relevant threshold ensuring complete vaporization of the inner liquid layer is defined. The dependence of this threshold with acoustical, geometrical, and mechanical parameters is also provided.

https://doi.org/10.1121/1.5019467

[CCC] Pages: 23–37

I. INTRODUCTION

Nanoparticles with a liquid core are receiving an increasing interest because of their potential medical applications such as contrast imaging, embolotherapy or targeted drug delivery.[1] Their size, typically a few hundreds of nanometers, and their stability thanks to their liquid core, allow them to circulate into the smallest capillary vessels, and also to extravasate towards tumoral tissues. Indeed, unlike normal blood vessels, tumor vessels are more permeable to well sized therapeutic agents:[2] this key mechanism is called the enhanced permeability and retention (EPR) effect.[3] Extravasation towards tumoral tissues can be enhanced by functionalizing particles with specific ligands.[4,5] Meanwhile, they can be made stealth to macrophages by means of PEGylated encapsulation.[6] Those particles are therefore a promising tool to circumvent some tumors' defense barriers and cargo anti-tumoral drugs as close as possible to target tissues. They can be dedicated to both diagnostic (contrast imaging) and therapy (drug cargos). Their medical functions can be mechanically activated by means of focused ultrasound. Actually, an adequate supply of acoustic energy can induce a phase change of the inner liquid:[1,7] this process is known as acoustic droplet vaporization (ADV). Ultrasound can be controlled to concentrate and localize the energy noninvasively but also to improve drug passage into tissue. ADV may then enhance echogenicity and turn nanoparticles into contrast agents for imaging within the tumor.[8] The volume expansion thus achieved can also occlude feeding blood vessels, reduce or even stop regional blood flow, and damage targeted tumors tissue: this process is known as embolotherapy.[9] Encapsulated bubbles can also carry drugs to be released specifically and selectively near tumoral cells, thus preserving healthy organs and reducing tumor cell resistance to anti-tumoral drugs. The drug might be placed inside the particle (within the liquid or trapped in an oiled phase) or attached to the shell material[8] depending on the therapeutic use. All these features are investigated with high interest since the early 2000s because they represent a promising way to treat malignant diseases.

The particles' content is necessarily made of biocompatible organic molecules, and perfluorocarbons (PFCs) are extensively considered. Encapsulated nanodroplets of PFCs can be obtained through nanoemulsions that succeed to provide calibrated particles.[10] PFCs are attractive candidate for ADV due to their physicochemical properties and especially the low boiling temperature of the lightest species, below human body temperature. Because of the additional Laplace pressure inside the droplet due to the surface tension, PFC droplets remain metastable at body temperature until a sufficient acoustic energy dose induces the vaporization.[1] Regarding the shell, encapsulation process generally favors the use of albumin layer,[9] polymeric shell,[11,12] phospholipids,[13] or fluorinated surfactants[14] to reach a sufficient lifetime for the droplet. Nevertheless, a trade-off is necessary between mechanical resistance of encapsulation to achieve stability, and compliance to enable vaporization. When the nucleation conditions are fulfilled, one or several small vapor bubbles of PFCs can be created within the liquid phase.[15] Furthermore, experimental *in vitro* studies suggest that the nascent bubble may collapse irremediably until its volume vanishes, or succeed to expand depending on the

[a]Electronic mail: thomas.lacour@upmc.fr

insonification characteristics,[7] and droplet geometry. Modeling the dynamics of the ADV process and exploring the minimum threshold required for vaporization is the objective of the present study, in order to provide the conceptual tool to optimize the ADV process, in terms of both mechanical properties of the encapsulating shell and acoustical parameters.

To reach this objective, the modeling of the acoustic droplet vaporization focuses on the radial dynamics of an initial vapor nucleus of perfluoropentane (PFP) originating in its liquid phase, surrounded by a nonlinear viscoelastic encapsulating material, itself immersed within an unbounded outer liquid. Considering a centered vapor seed is a common assumption that remains valid for submicrometric droplet[15,16] ($\lesssim 1\,\mu$m) and that obviously simplifies the modeling. It is worth noting that all theoretical models investigating ADV rely, for the sake of simplicity, on the assumption of spherical symmetry, even though recent ultrafast optical measurements indicate more complex geometries may occur such as toroidal deformation[15] or multiple nuclei.[17]

The dynamical behavior of a spherical cavity originates from the work of Besant[18] and was later applied to the context of cavitation damage by Lord Rayleigh.[19] These basic models have since been generalized to take into account various properties of the cavity environment: surface tension,[20] viscosity,[21] heat diffusion,[20,22] compressibility.[23] The related model of ADV starts with the growth description of a single bubble in a pure liquid-vapor system. This has already been modeled[24] and compared with ultrafast optical imaging[25] for droplets with initial radii on the order of a few micrometers. Indeed, high-speed optical microscopy cannot observe a single droplet on the order of a few hundreds of nanometers. For micrometric droplets, the focusing effect of the droplet itself, especially if the exciting signal is nonlinearly distorted with superharmonic content, has also been shown necessary to take into account.[26,27] Influences of heat transfer[16,28] and of dissolved inert gases[16] have also been theoretically described and compared favorably to experiments. Nano- or micro-particles have recently been considered as a vapor bubble within a liquid layer of finite thickness.[13] However, a realistic representation of such particles during the ADV process requires one to incorporate into the model the mechanical effects of the encapsulating shell, thus leading to a four-phase model (vapor + liquid + shell + surrounding environment). A complete formulation for the vapor bubble dynamics in an encapsulated droplet has recently been proposed in the case of linear elasticity for the shell rheology,[29] combining the previously reviewed models of vapor bubble growth, with a well-known description of contrast agent encapsulation.[30]

However, linear elasticity approximation turns out to be too restrictive regarding the large shell deformations resulting from the liquid to vapor phase change (typically a fivefold radius increase[31] for the PFP). Several models for shell nonlinear behavior are available in the literature for ultrasonic contrast agents. Nevertheless, these models are limited to the case of an interface whose thickness is assumed negligible with respect to the particle size.[32–34] In this context, the first objective of the present paper is to generalize the previous model (Ref. 29) in order to handle such large deformations by incorporating nonlinear elasticity in the shell rheology. This is based on the well-known strain-softening material behavior of Mooney-Rivlin material,[35,36] well adapted to very large deformations (several hundreds of percent) of nearly incompressible materials. Indeed, harder shell components for which the Mooney-Rivlin model assumptions are invalid, would turn out too rigid for an efficient ADV process anyways.

Section II summarizes the theoretical formulation, first accounting for phase change at the liquid-vapor interface (Sec. II A), before incorporating shell elastic nonlinearities (Sec. II B). For the PFP vapor/PFP/shell/water system described in Sec. III, various responses to ultrasound excitation will be illustrated in Sec. IV, depending on linear and nonlinear mechanical shell properties and acoustical excitation parameters. The second objective is to open ways to elucidate the key question of ADV threshold for optimization of nano- or micro-droplets design or/and acoustical parameters. This is the purpose of Sec. V which exhibits different classes of ADV outcomes and defines a relevant threshold ensuring complete vaporization of the inner liquid layer. The dependence of this threshold with acoustical and geometrical parameters will finally be investigated.

II. THEORETICAL MODEL

A. Vapor bubble dynamics

A spherical inviscid vapor bubble with a dynamical radius $R(t)$ is centered in its viscous liquid phase (inner liquid) as schematized in Fig. 1. This two-phase content constitutes a metastable mixture of liquid and vapor. We consider here especially perfluoropentane (C_5F_{12}), which is an attractive PFC candidate for its low boiling temperature (29 °C at 1 atm) below body temperature. This droplet is encapsulated within a spherical incompressible viscoelastic shell with inner $a(t)$ and outer $b(t)$ dynamical radii immersed in an unbounded incompressible viscous liquid free of body force (external liquid). Incompressibility assumptions are justified by the small size of the droplet (typically 100 to 1000 nm) much smaller than the acoustic wavelength (larger than 0.3 mm for medical frequencies considered here smaller than 5 MHz), and by the even smaller shell thickness. Shell compressibility has to be considered only for thick and hard layers,[37] a case not considered here as such shells would prevent ADV at sufficiently low acoustical pressure levels.

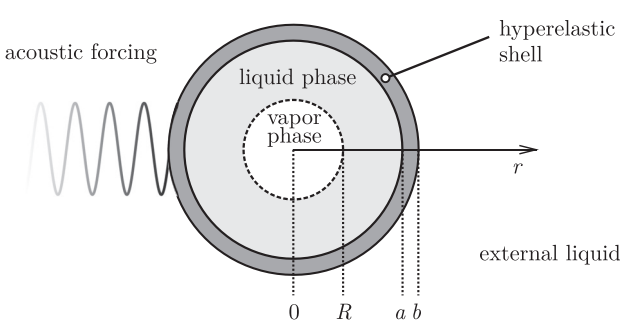

FIG. 1. Schematic sketch of the geometry.

Initial radii are denoted by a_0 and b_0, respectively, for the inner and outer shell interfaces. It is assumed there is no mass exchange at the shell interfaces $r=a$ and $r=b$. This is justified by the timescales considered here, on the order of microseconds, which are much shorter than the reported timescales for mass diffusion[7,38] on the order of at least milliseconds. For the present geometry, the subscripts V, L, S, and E will denote quantities relative to the vapor phase, inner liquid phase, shell, and external liquid, respectively. From mass conservation, incompressibility assumption, and spherical symmetry, the radial velocity u outside the bubble at distance $r>R$ from the center satisfies[19]

$$u(r,t) = (R/r)^2 U(t), \tag{1}$$

where $U = U_{\mathrm{L}}$ is the radial velocity in the liquid at the bubble interface $r=R$. Because of the mass flux J across the surface $r=R$, the radial velocity of the inner liquid near the bubble wall is not identical to $\dot{R}$. The mass flux occurs during condensation and evaporation, namely,[28,39]

$$J = \rho_{\mathrm{L}}(U_{\mathrm{L}} - \dot{R}) = \rho_{\mathrm{v}}(U_{\mathrm{V}} - \dot{R}), \tag{2}$$

with U_{V} the vapor velocity at $r=R$ and ρ_{V} the vapor density which depends on the bubble surface temperature θ_{V}. Regarding the small size of the bubble and the ratio of heat diffusion coefficient between the liquid and vapor phases, the vapor phase is commonly assumed of uniform pressure, temperature, and density.[28] Moreover, it satisfies the perfect gas law $\rho_{\mathrm{V}} = p_{\mathrm{V}}/(r_{\mathrm{V}}\theta_{\mathrm{V}})$, where r_{V} is the specific gas constant of the vapor (equal to 28.8 $\mathrm{J\,kg^{-1}\,K^{-1}}$ for PFP). Using relation (1), the radial component of the momentum equation for $r \geq R$ reduces to

$$\frac{R^2\dot{U}}{r^2} + \frac{2R\dot{R}U}{r^2} - \frac{2R^4U^2}{r^5} = \frac{1}{\rho}\frac{\partial \mathrm{T}_{rr}}{\partial r} + \frac{3}{\rho}\frac{\mathrm{T}_{rr}+p}{r}, \tag{3}$$

where ρ is density, $p = -(\mathrm{tr}\,\mathbf{T})/3$ is the hydrostatic pressure associated to the internal constraint of incompressibility, and T_{rr} is the radial component of the stress tensor $\mathbf{T}$. Equation (1) for velocity and Eq. (3) for momentum are valid within inner liquid, shell, and external liquid. The density is constant in each of these three layers. The radial component of the stress tensor is postulated to be the sum of a viscous part $\mathrm{T}^{\mathrm{v}}_{rr} = 2\eta(\partial u/\partial r) = -4\eta UR^2/r^3$ and an elastic part $\mathrm{T}^{\mathrm{e}}_{rr}$. Assuming both liquids behave as Newtonian fluids ($\mathrm{T}^{\mathrm{e}}_{rr,\mathrm{E}} = \mathrm{T}^{\mathrm{e}}_{rr,\mathrm{L}} = 0$), only the shell has a non-zero elastic part $\mathrm{T}^{\mathrm{e}}_{rr,\mathrm{S}}$. The latter differs from previous works[29,30] as nonlinearities have to be taken into account due to the large droplet growth occurring because of the vapor bubble expansion. The shell is assumed to act like a Kelvin-Voigt material with a non linear spring (the elastic part) in parallel with a linear dashpot (the viscous part). Integrating Eq. (3) in the different layers out of the bubble from $r=R$ to $r=+\infty$ with boundary conditions at the three interfaces ($r=R$, $r=a$, $r=b$), the following generalized Rayleigh-Plesset equation for the bubble dynamics is obtained:

$$R\dot{U} + \frac{4\xi - (\Gamma_4/\Gamma_1)\xi^2}{2}\dot{R}^2 = \frac{p_R - p_\infty}{\Gamma_1}, \tag{4}$$

where Γ_i ($i=1, 4$) are coupling coefficients, $\xi = U/\dot{R}$. The resulting pressure p_R at the liquid-vapor interface $r=R$ is given by

$$p_R = p_{\mathrm{V}} - \frac{2\bar{\sigma} + 4\bar{\eta}U}{R} + \Phi + \mathcal{S}, \tag{5}$$

while the pressure at infinity in the outer liquid is p_∞. This driving pressure is the sum of the static pressure p_0 and an acoustic component p_a with angular frequency ω. We choose $p_a(t) = -P\sin\omega t$ $(t>0)$ to get initial expansion when acoustic excitation is turned on. This choice is discussed in Appendix B.

Note that, the waveform distortion that amplifies peak positive pressures, shortens compression phase, and broadens rarefaction for moderate-to-high excitation pressures used in nearly all droplet studies [see, for instance, Fig. 5(b) in Ref. 27], is not investigated here for the sake of simplicity. Moreover, Shpak *et al.*[26] demonstrated the influence of nonlinear harmonics focusing by the droplet itself (so-called "superharmonic focusing") on the threshold for nucleation. We can remark, however, that according to this study the influence of superharmonic focusing is most sensitive for droplets larger than a few micrometers. As both effects would add new parameters in our study, we do not consider here such a complex excitation that would deserve further investigations. Especially, the nonlinear waveform distortion would need special attention as it would impact droplets of any size.

In Eq. (5), the coefficient $\bar{\sigma}$ is an effective surface tension, $\bar{\eta}$ is an effective viscosity, while Φ represents the contribution due to the mass flux J and $\mathcal{S} = 3\int_a^b (\mathrm{T}^{\mathrm{e}}_{rr,\mathrm{S}} + p)\mathrm{d}r$ describes the shell elastic response (see Sec. II B for more details). Coupling coefficients ($i=1, 4$), viscosity contribution and effective surface tension are, respectively, given by the relations

$$\Gamma_i = \rho_{\mathrm{L}} + (\rho_{\mathrm{S}} - \rho_{\mathrm{L}})(R/a)^i + (\rho_{\mathrm{E}} - \rho_{\mathrm{S}})(R/b)^i, \tag{6a}$$

$$\bar{\eta} = \eta_{\mathrm{L}} + (\eta_{\mathrm{S}} - \eta_{\mathrm{L}})(R/a)^3 + (\eta_{\mathrm{E}} - \eta_{\mathrm{S}})(R/b)^3, \tag{6b}$$

$$\bar{\sigma} = \sigma + \sigma_1(R/a) + \sigma_2(R/b). \tag{6c}$$

For simplicity, the surface tensions σ_1 and σ_2 associated with internal and external curvature of the shell are assumed to be negligible so that $\bar{\sigma} \simeq \sigma$. The coefficient Γ_1 is the effective density of the domain outside the bubble. It is an analogue to the external liquid density involved in the classical form of Rayleigh-Plesset equation for a spherical cavity in an incompressible fluid free of body force and mass transport across the interface[19] (free bubble geometry). In the present geometry, a growing of the vapor bubble yields to a decreasing apparent density Γ_1 (Fig. 2 left). The coefficient before $\dot{R}^2$ depends on both Γ_i and ξ in the generalized form Eq. (4). But assuming $\xi \approx 1$ this coefficient is equal to 3/2 when $R \ll 1$ or $R=a$ (Fig. 2 right) so that inertial part of Eq. (4) is consistent with the one involved in the classical Rayleigh-Plesset equation[19] $R\ddot{R} + (3/2)\dot{R}^2$. It should be noted that for the present case of thin shell ($a \approx b$), the Γ_i coefficients mostly vary due to the density contrast between inner and outer liquids and $\Gamma_i \approx \rho_{\mathrm{L}} + (\rho_{\mathrm{E}} - \rho_{\mathrm{L}})(R/a)^i$.

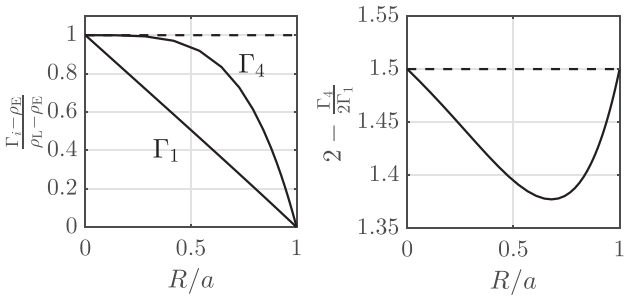

FIG. 2. Variation of inertial coupling coefficients Γ_i normalized (left) and of the coefficient in front of $\dot{R}^2$ in Eq. (4) with $\xi = 1$ (right). Dashed lines correspond to the particular case $\rho_L = \rho_E$ equivalent to a bubble in an unbounded liquid. Values use for density are collected in Table I.

Assuming thermodynamical equilibrium (saturation condition) and a heavy liquid phase relative to its vapor $\rho_L \ll \rho_V$, the vapor pressure p_V is given by the Clausius-Clapeyron law[28,40]

$$\frac{\mathrm{d}p_V}{\mathrm{d}\theta_V} \approx \frac{L}{r_V}\frac{p_V}{\theta_V^2}, \tag{7}$$

where L is the latent heat of vaporization (independent of θ_V). Using the perfect gas law, the phase change of liquid PFP droplet can be estimate. Assuming that the whole mass of liquid PFP turns into vapor without any loss, then the relative change in volume is $(R_{\text{final}}/a_0)^3 = \rho_L/\rho_V$. Furthermore, assuming the system after complete vaporization to be nearly isothermal at the temperature $\theta_{E,\infty}$ far from the bubble vaporization, the final bubble radius after complete vaporization is

$$R_{\text{final}} = a_0\sqrt[3]{r_V\theta_{E,\infty}\rho_L/p_V(\theta_{E,\infty})} \approx 4.8a_0. \tag{8}$$

The shell radius would thus increase almost fivefold to enable the maximum expansion of the vapor phase and the total vaporization of the inner liquid. A similar ratio (≈5.22) would be obtained for perfluorobutane (C_4F_{10}) which is also a good candidate for ADV because of its very low boiling point (−1 °C) or for other PFCs like perfluorohexane (C_6F_{14}), which is less appealing because of its higher boiling point (56 °C) above body temperature.

The mass flux contribution $\Phi = J(U_V - U)$ in Eq. (5) arises from the evaporation process. It appears by writing the continuity of the normal stress[41] $\mathrm{T}_{rr,V} + JU_V = \mathrm{T}_{rr,L} + JU + 2\sigma/R$ at the liquid-vapor interface ($r = R$). With Eq. (2), the contribution Φ is reduced to

$$\Phi = J^2(\rho_V^{-1} - \rho_L^{-1}). \tag{9}$$

Furthermore, the mass flux J can be approximated from continuity of the energy flux by neglecting viscous dissipation for the inner liquid and by considering adiabatic process for the vapor phase.[42] Consequently $J \simeq q_L/L$, where q_L is the radial heat flux in the liquid at the bubble surface $r = R^+$. Generalized Rayleigh-Plesset Eq. (4) has to be completed by the diffusion equation for temperature in the liquid phases, neglecting thermal dissipation in the shell. This provides the heat flux q_L, and therefore the mass flux J. Neglecting viscous and thermal losses in the vapor phase, the conservation of energy leads to the following differential equation governing the bubble surface temperature:[13]

$$\frac{L}{r_V}\frac{\dot{\theta}_V}{\theta_V^2} + \frac{3\gamma}{R}\left(\frac{q_L}{\rho_V L} + \dot{R}\right) = 0, \tag{10}$$

where $\gamma = 1.05$ is the ratio of specific heats of the vapor.[13] The reader is referred to Ref. 29 for further details on the numerical resolution.

B. Shell elasticity

The terms in the pressure p_R are almost entirely explained. The elastic response $\mathcal{S}$ of the shell given by

$$\mathcal{S} = 3\int_a^b \frac{\mathrm{T}^{\mathrm{e}}_{rr,S} + p}{r}\mathrm{d}r \tag{11}$$

remains to be defined. To close the formulation, a constitutive law for the stress/strain dependence must be assumed. Nonlinearities are indeed expected to be important due to large deformations of the shell. The corresponding stress is fully determined by the class of materials used to model the shell elastic behavior. Assuming the shell is sufficiently thin compared to the particle outer radius, which itself is much smaller than the wavelength, it is a very good approximation to consider the shell material as an incompressible viscoelastic solid.[37] The modeling of the elastic part is based on the point of view of continuum mechanics in finite transformations.[43] The shell is assumed to be an isotropic and incompressible hyperelastic body deforming while keeping its spherical symmetry. The coating shell is also assumed to keep on covering homogeneously the bubble/droplet system all over the ADV process despite the undergone very large deformation. The rupture of the shell is thus not considered here. This assumption is justified by observations indicating that some coating materials (like phospholipids) remain after vaporization, though others (albumin) cover the bubble only partially, in heterogeneous patches.[44] The shell motion is represented by the relation $\mathbf{x} = \boldsymbol{\chi}(\mathbf{X}, t)$, where $\mathbf{X} = r_0\mathbf{e}_r$ denotes the coordinates in the reference configuration of a point whose actual coordinates are $\mathbf{x} = r(r_0, t)\mathbf{e}_r$, $\boldsymbol{\chi}$ being a bijective mapping function. Vector $\mathbf{e}_r$ is the unit vector in the radial direction. For two sufficiently close points that experience a finite transformation, all the derivatives are supposed to be meaningful and the first order deformation gradient $\mathbf{F}(\mathbf{X}, t) = \partial\boldsymbol{\chi}/\partial\mathbf{X}$ has the following nonzero components:

$$\mathrm{F}_{rr} = \partial r/\partial r_0 \quad \text{and} \quad \mathrm{F}_{\theta\theta} = \mathrm{F}_{\phi\phi} = r/r_0 = \lambda, \tag{12}$$

where λ is the ratio between the radial coordinates at inflated and uninflated states. A hyperelastic body is associated with a strain energy density function, denoted $\Psi = \Psi(\mathbf{F})$, that characterizes the way the shell material stores elastic energy while undergoing a deformation. This function is subject to the principle of frame indifference.[45] For an elastic material, the stress tensor is explicitly $\mathbf{T}^{\mathrm{e}}_{\mathrm{S}} = \mathbf{F}\partial\Psi/\partial\mathbf{F}$. Because of

incompressibility assumption, the volume conservation requires that the Jacobian of the transformation satisfies $\det \mathbf{F} = 1$ at all times. This implies that

$$\partial r/\partial r_0 = (r_0/r)^2, \tag{13}$$

so that $r^3 = r_0^3 + \delta^3(t)$, which can also be written as follows:

$$\lambda(r,t) = (1 - \delta^3/r^3)^{-1/3}, \tag{14}$$

where $\delta^3(t) = a^3(t) - a_0^3 = b^3(t) - b_0^3$. The deformation gradient being $\mathbf{F} = \mathrm{diag}\,(\lambda^{-2}, \lambda, \lambda)$, the stress tensor is reduced to a diagonal matrix[43] and the energy only depends on the principal stretch λ (circumferential stretch). The radial component of the shell elastic stress tensor may be separated into a deviatoric part $\mathrm{T}^{\mathrm{e}}_{rr,\mathrm{S}} - \mathrm{tr}(\mathbf{T}^{\mathrm{e}}_{\mathrm{S}})/3$ and a spherical part $p = -\mathrm{tr}(\mathbf{T}^{\mathrm{e}}_{\mathrm{S}})/3$ so that[45]

$$\mathrm{T}^{\mathrm{e}}_{rr,\mathrm{S}} = -p - \frac{1}{3}\lambda\Psi'(\lambda). \tag{15}$$

The pressure p is an internal strain arising from incompressibility condition and the prime denotes the first derivative with respect to λ. Replacing the radial component (15) in Eq. (11) and noting that $\mathrm{d}\lambda/\mathrm{d}r = (\lambda - \lambda^4)/r$ leads to

$$\mathrm{d}\mathcal{S} = \frac{\Psi'(\lambda)}{\lambda^3 - 1}\mathrm{d}\lambda, \tag{16}$$

a relation equivalent to Eq. (2.11) of Ref. 46 describing the inflation of rubber balloons. Relation (16) is fundamental to express the elastic stress in the generalized Rayleigh-Plesset Eq. (4). To figure out how the shell reacts to a mechanical stress, it is necessary to focus on the mathematical form of the energy Ψ.

In the literature, a wide variety of formulations that estimate the strain energy density exists. The common approach leads to a Taylor expansion of Ψ that involves algebraic spatial invariants and elastic constants. Because of symmetry arguments, the maximum number of independent invariants is three for an isotropic body, and is reduced to 2 for an incompressible material. In addition to those invariants, some mathematical considerations show that incompressibility requires exactly the same number of independent elastic constants as the order of approximation with respect to strain measurement.[47] A straightforward extension of the linear constitutive law is the Saint Venant-Kirchhoff material that assumes a linear stress–strain relation, with geometrical nonlinearities arising only from the nonlinear strain–displacement relation. In this case, Ψ is expanded only up to the second order of the deformation and depends on the invariants of the Green-Lagrange strain tensor $\boldsymbol{e} = (\mathbf{F}^t\mathbf{F} - \mathbf{I})/2$, namely, $\Psi = GL_2$, where G is the linear shear modulus and $L_i = \mathrm{tr}(\boldsymbol{e}^i)$ $(i = 1, 2, 3)$ is the set of invariants defined by Landau. When expanding the energy to the next order, the material nonlinearities appear through an additional term proportional to Landau[48] third order elastic constant $\mathcal{A}$ and $\Psi \simeq GL_2 + \mathcal{A}L_3/3$. This truncature is problematic for negative values of $\mathcal{A}$ for which one may get $\Psi < 0$. Indeed, the term L_3 becomes dominant when $|\lambda|$ exceeds a critical value so that the energy has the same sign as $\mathcal{A}$. This form has therefore to be disregarded, because experimental measurements reveal that $\mathcal{A}$ is negative for many materials such as steel,[49] inviscid fluids,[50] and soft solids.[51] Increasing the order of approximation to fourth order would allow us to use negative values but this would introduce a new elastic constant and therefore an additional unknown parameter to handle [Eq. (23) in Ref. 52]. Another approach is to include material nonlinearities through a phenomenological polynomial expansion of Ψ depending on the invariants of $\mathbf{b} = \mathbf{F}\mathbf{F}^t$ (left Cauchy-Green tensor). In order to favor the deformation of the shell, the rheology must preferably be of the "strain-softening" kind, with the apparent elastic modulus decreasing with deformation. A first order approximation, linear with respect to these invariants of $\mathbf{b}$, is the Mooney-Rivlin stored-energy function for an incompressible solid[35]

$$\Psi \simeq \frac{G}{4}\sum_{i=-1}^{1}(1 + i\beta)I_i, \tag{17}$$

where β is a nonlinear coefficient that satisfies $\beta = 3 + \mathcal{A}/2G$ [see Eq. (64) in Ref. 53]. This form of stored energy function is reliable on the range $1 \leq \lambda < 5$, therefore suitable for the expected stretch after complete vaporization of the droplet.[35] The invariants I_i are scalar functions of the principal stretch λ given by

$$I_i(\lambda) = \mathrm{tr}\,(\mathbf{b}^i) - 3 = \lambda^{-4i} + 2\lambda^{2i} - 3. \tag{18}$$

These invariants I_i have the advantage of being connected to basic geometric quantities. Actually, I_1 is related to the square of the stretch ratio on an infinitesimal line element averaged over all possible orientations and I_{-1} to the stretch ratio on an infinitesimal area element averaged over all possible orientations.[54] Because of incompressibility assumption, these invariants are associated with two reciprocal deformations (an increased shell surface leads to a decreased thickness and vice versa) so that $I_1(1/\lambda) = I_{-1}(\lambda)$. Consequently, the coefficient β turns out as a measure of the relative importance of these reciprocal deformations and is called an asymmetry coefficient by Mooney.[35] As mentioned earlier, there are only two independent invariants for incompressible isotropic materials and it should be noted that I_i and L_i are related to one another. Expression (17) allows negative values for $\mathcal{A}$, but to ensure the positivity of Ψ, the partial derivatives $\partial\Psi/\partial I_i$ $(i = -1,1)$ have to be positive. The nonlinear coefficient is therefore restricted to the range $-1 < \beta < 1$ and consequently, the third-order elastic constant $\mathcal{A}$ lies in the range

$$-8G < \mathcal{A} < -4G. \tag{19}$$

To account for Mooney-Rivlin behavior of the shell in the Rayleigh-Plesset Eq. (4), the derivative of the strain energy density function has to be evaluated and then the relation (16) has to be integrated to give

$$\mathcal{S} = 2G\left[\sum_{\substack{i=-1\\ i\neq 0}}^{1}\sum_{k=0}^{1}\frac{1 + i\beta}{-i - 3k}\lambda^{-i-3k}\right]_{\lambda=a/a_0}^{\lambda=b/b_0}. \tag{20}$$

Details for obtaining above expression are provided in Appendix A. Linear elasticity can be recovered from Saint Venant-Kirchhoff and Mooney-Rivlin material. Under the assumption of small displacements $\delta^3/r^3 \ll 1$, the principal stretch can be approximated by

$$\lambda^k = 1 + k\delta^3/3r^3. \tag{21}$$

The resulting linear Hooke elastic stress

$$\mathcal{S}_0 = \frac{4}{3}G\left[\frac{\delta^3}{r^3}\right]_{r=a}^{r=b} \tag{22}$$

is deduced, consistently with previous works.[29,30] Resulting elastic stress $\mathcal{S}$ normalized by the linear one $\mathcal{S}_0$ is displayed in Fig. 3. The theoretical deformation expected for the complete vaporization is, in particular, highlighted. For small displacements, all models are equivalent, in agreement with Hooke's law. When the shell undergoes a greater deformation ($a > 1.25a_0$) caused by the expansion of the vapor phase, the different rheologies react differently. The Mooney-Rivlin one gives a stress ranging between one ($\beta = 1$) and two ($\beta = -1$) magnitudes greater than linear elasticity. Neglecting nonlinearities clearly tends to artificially make the system softer and consequently to ease the shell inflation and the vaporization. As soon as $\beta > -1$ the elastic response of a Mooney-Rivlin material gets softer. In order to optimize the bubble growth, the variation of S associated with the deformation suggests that the shell material should ideally behave as the softest Mooney-Rivlin material with $\beta = 1$, which corresponds to the class of neo-Hookean solids[55] depending only on the invariant I_1.

III. CHOICE OF PARAMETERS

The vapor radial dynamics is numerically simulated for a micrometric droplet of perfluoropentane (PFP) C_5F_{12} immersed in water at human body temperature 37 °C and atmospheric pressure. At initial time, the shell inner radius is $a_0 = 1$ μm and its thickness is $h_0 = b_0 - a_0 = 10$ nm. The

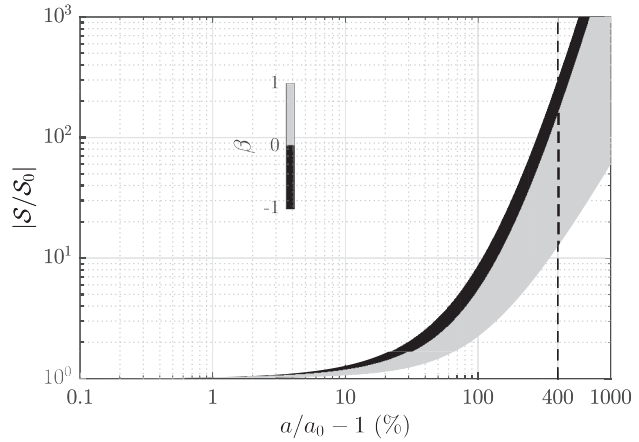

FIG. 3. Nonlinear Mooney-Rivlin elastic response normalized by the linear one. Gray colormap indicates the value of β nonlinear parameter. Thin vertical line at 400% denotes the deformation expected after complete vaporization of the PFC liquid core.

particle size, content, and thermophysical parameters are chosen to be consistent with previous studies[13,29] and are collected in Table I. Even if the vapor behavior is strongly dependent on the size of the initial vapor nucleus, it is arbitrarily fixed to $R(t = 0) \simeq 80$ nm in the following simulations, unless specified otherwise (see Secs. IV and V), to focus on the shell mechanical properties. This value is chosen to be below the critical radius of unstable equilibrium[20]

$$R^\star = 2\sigma/\left[p_V(\theta_{v,\infty}) - p_0\right]. \tag{23}$$

A nucleus larger than $R^\star$ would spontaneously grow while a smaller one would spontaneously collapse in the absence of acoustical excitation. Shell mechanical properties (G and β parameters) are here considered as free parameters. In our simulations, the product Gh_0 is, however, limited to the maximum value 5 N/m ($G = 480$ MPa in Fig. 6). Such high values of shear modulus are more adapted to describe soft polymer shells, though much stiffer polymers have also been considered for encapsulation, for instance, poly lactic-co-glycolic acid (PLGA) with shear modulus on the order of 3 GPa.[14] However, such stiff encapsulation turns out unfavorable for the ADV process, which justifies our choice to consider smaller G values. At least in the linear regime, the product Gh_0 is also a good measurement for surface tension that could describe encapsulation by phospholipids. In this case, the typical values for Gh_0 are not much larger than 1 mN/m, which amounts to $G < 1$ MPa (see, for example, Table I in Ref. 34). It will be shown (see Sec. V) that such low values induce a weak mechanical influence of the encapsulation. However, the assumption of incompressibility will lead to a very thin layer after vaporization, which may not perfectly represent the behavior of surfactants. We rather expect an enlargement of the interspace between the shell molecules with a more or less constant layer thickness. Alternative models considering a variable surface tension[34,57] would be in this case more suitable and are currently considered in ongoing studies. The value of density $\rho_S = 1100$ kg m^{-3} is chosen slightly higher than that of water and cells[30] for a soft material. Actually, for a small thickness $b - a$ compared to the radius a, the shell inertia is negligible in the bubble dynamics (see $\rho_E = \rho_L$ dashed lines in Fig. 2). Regarding numerical parameters, the simulations are stopped when either the inner liquid layer is zero at machine precision (typically 10^{-14} nm for total vaporization, see Fig. 4), or the vapor bubble nucleus is smaller than $R_0/100$ nm for collapse. Note our numerical model could

TABLE I. Parameters used in numerical simulations. K stands for the thermal conductivity and c for the isochoric specific heat per unit mass.

	Interface (Ref. 56)	Liquid (PFP)	Shell (Ref. 30) (Parametric)	External (water)
	—			
ρ (kg m^{-3})		1630 (Ref. 56)	1100	998
η (mN s m^{-2})		0.652 (Ref. 56)	50	1
K (W m^{-1} K^{-1})		0.056 (Ref. 13)		0.6
σ (mN m^{-1})	9.5			
L (kJ kg^{-1})	88			
c (J kg^{-1} K^{-1})		1089 (Ref. 13)		4200

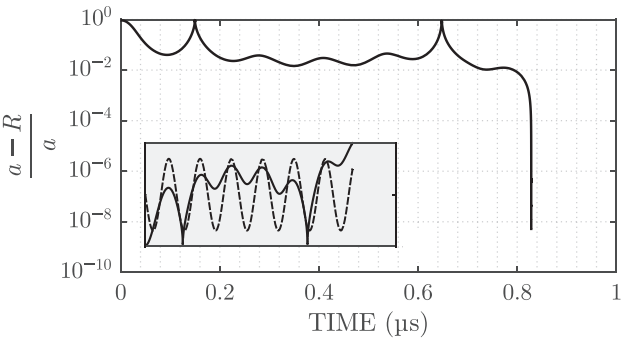

FIG. 4. Normalized inner liquid thickness $(a-R)/a$ history (solid line), applied acoustic pressure of 3.64 MPa at 5 MHz (for $\beta=1$ and $G=20$ MPa). Small box: corresponding bubble radius history and acoustic excitation (dashed line).

not consider the case of a completely vaporized droplet that condenses back during the acoustic compression phase. Although we cannot rule such a re-condensation event, it has not been observed experimentally in the work of Doinikov *et al.*[13] Moreover, spontaneous re-condensation process has been recently observed for perfluorohexane nanodroplets with a boiling point (56 °C) above body temperature thus leading to so-called "blinking droplets" activated by laser excitation.[58,59] The heat diffusion equations are transformed by introducing new spatial coordinates which allow us to fix the moving boundaries [$r=R(t)$ and $r=b(t)$]. The resulting equations are discretized with 32 points per diffusion length, by centered (except at the boundaries) second order finite differences. Time evolution is solved by a numerical solver adapted for stiff differential equations (see Ref. 29 for more details). An example of numerical simulation illustrating the bubble radius evolution over several acoustic cycles is displayed on Fig. 4. In this case, the bubble radius reaches six maxima and approaches collapse twice before complete vaporization. One can notice that the bubble expansion and compression phases are partly out of phase with the acoustic excitation, as the bubble radius reaches a local maximum more or less at the peak of acoustic compression. Similar bubble dynamics has already been observed experimentally, see, for instance, Fig. 2 in Ref. 16.

IV. BUBBLE BEHAVIORS

A. Influence of acoustic amplitude

Numerical simulations reveal different bubble outcomes according to the shell elasticity and the acoustic excitation. Figure 5 displays the bubble radius as a function of time for selected acoustic pressures associated with noteworthy dynamics. When applied amplitude excitation is increased at a given frequency, the bubble history exhibits at least three distinct behaviors. If the amplitude of acoustic excitation is below a critical value, the vapor nucleus spontaneously shrinks as the acoustic excitation is too low to counterbalance its natural trend to collapse. This is defined as regime I. On the contrary, for the largest amplitude (Fig. 5 with $P=5$ MPa), the initial trend to collapse is quickly counterbalanced by the applied negative pressure. Then the vapor bubble grows monotonically until complete vaporization:

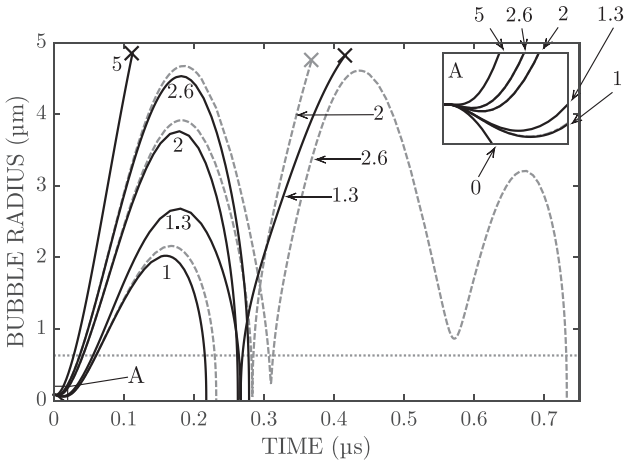

FIG. 5. Radius R of vapor bubble *vs* time curves for 6 excitation amplitudes P (0, 1, 1.3, 2.6, and 5 MPa at a given frequency $f=4$ MHz. Solid lines are associated with a Mooney-Rivlin material with $\beta=1$ and dashed lines with linear elasticity. The shear modulus value of the shell is $G=20$ MPa. The initial droplet size is $a_0=1$ μm and the initial bubble radius is $R_0=80$ nm. The small graph represents a zoomed view from 0 to 0.02 μs. Figures indicate the pressure excitation. Horizontal dotted-line shows the critical radius $R^\star$.

this is regime III. Note that the two shell material behaviors (linear or Mooney-Rivlin) are indistinguishable in these two regimes. Between these two extremal behaviors, the radius first decreases according to its natural trend to collapse [see (A) in Fig. 5], then increases under the action of acoustic pressure up to a maximum value. However, the acoustic pressure level is not sufficient to reach the complete vaporization during the first acoustic expansion phase (0.125 μs). A competition begins between the applied compression phase and the natural trend of the bubble to grow as it is now beyond its critical radius $R^\star$ (indicated by the horizontal line in Fig. 5). Then various outcomes may occur in numerical simulations depending on the amplitude of excitation applied and the shell rheology employed. This regime with at least one local maximum of the radius is called regime II. The vapor bubble can collapse and rebound one or several times before irremediably shrinking (dashed line at 2.6 MPa in Fig. 5 with two rebounds) or finally it reaches a state of complete vaporization (at 2 MPa in the linear case or 1.3 MPa for nonlinear case, as visible in Fig. 5).

B. Influence of shell elasticity

At the same acoustical parameters, if the material rheology switches to nonlinear elasticity, bubble outcomes are rather different and the complete vaporization is not observed anymore for the same excitation pressures (Fig. 5, 2 and 2.6 MPa, solid lines). This indicates a sensitivity of the bubble ultimate fate with regard to the shell nonlinear elastic properties: a Mooney-Rivlin behavior induces higher shell stiffness as previously outlined in Fig. 3 and therefore leads to bubble collapse whereas it would vaporize in the linear case. A threshold for applied acoustic amplitude p_{th} above which vaporization is achieved *without any rebound* can therefore be defined. This threshold depends, among others, on frequency and initial bubble radius.

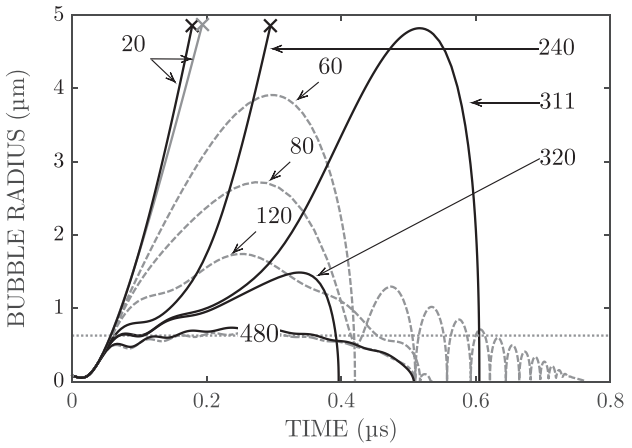

FIG. 6. Numerical solutions for bubble radius as a function of time for various shear moduli G, at a given excitation frequency $f = 1$ MHz and a pressure amplitude $P = 4$ MPa. Continuous lines denote the use of a Mooney-Rivlin model for the shell material with $\beta = 1$ and the dashed lines correspond to $\beta = -1$. The value of the initial droplet size is $a_0 = 1$ μm and the initial bubble radius is $R_0 = 80$ nm. Arrows indicate the value of the shear modulus G. Horizontal dotted-line shows the critical radius $R^\star$.

But the level of nonlinearities also plays a significant role on the vapor bubble dynamics. Figure 6 illustrates the bubble radius history for two encapsulations with a Mooney-Rivlin material for the two extreme values of nonlinear parameter β. It also underlines the importance of the shear modulus on the vaporization process at a given acoustical excitation. For hard shells ($G = 480$ MPa), the vapor nucleus succeeds to initially grow, but it then smoothly oscillates around its critical radius $R^\star \approx 0.63$ μm (identified by horizontal line in Fig. 6) and finally shrinks, without noticeable variations between the cases $\beta = 1$ and $\beta = -1$. Soft shells ($G = 20$ MPa) ensure the complete vaporization and for this low rigidity, the nonlinear parameter β slightly affects the characteristic time required for the entire vaporization. On the contrary, the intermediate behaviors depend on the choice of β. The numerical simulation indicates that the vaporization occurs in a large range of G ($G < 310$ MPa) for the case $\beta = 1$ (solid lines in Fig. 6). On the contrary for the case $\beta = -1$, the process is inhibited for a shear modulus as low as $G = 60$ MPa (dashed lines in Fig. 6). This confirms the evolution of the normalized elastic response $\mathcal{S}/\mathcal{S}_0$ in Fig. 3, where the nonlinear elastic response is separated by almost one order of magnitude between the two extreme values of β in the deformation range $a/a_0 < 5$. The coefficient β appears in fact as a stiffness measurement associated with material nonlinearities. When $\beta = -1$ (dashed lines in Fig. 6), a shear modulus value $G = 80$ MPa produces an oscillating regime with several rebounds, with a decreasing maximum radius between two consecutive ones, continuing until the vapor bubble finally vanishes. Obviously, the predicted rebounds and collapses from numerical results in Figs. 5 and 6 should be carefully interpreted because they are associated with high temperature and high liquid-vapor interface speed. Even if rebounds are observed experimentally,[13,16] such conditions may not be compatible with the incompressibility and the thermodynamical equilibrium assumptions used in the present model. This enforces our choice for the unambiguous definition of the acoustic vaporization threshold as being the minimal pressure required to reach the numerical outcome $R = a$ without rebounds (regime III).

V. DIRECT VAPORIZATION THRESHOLD

A. Definition and computation

As shown in Sec. IV, the numerical simulations predict different ends of life for the bubble dynamics that can be sorted at least into three families. Compared to the case of a vapor bubble in an unbounded liquid, the confinement within a shell introduces an upper limit in that growth and condition $0 < R < a$ must be satisfied at all times. The direct threshold p_{th} is defined as the minimum acoustic pressure for which complete vaporization is achieved without any rebounds (regime III). This threshold should be here clearly distinguished from the more usual nucleation threshold[27,60,61] required to nucleate the vapor bubble from an unperturbed liquid droplet with no gas. Direct threshold is computed numerically by solving the nonlinear system and searching for the minimum pressure that leads to the regime III at a given frequency. Starting from a given maximum excitation level, a dichotomy iterative algorithm is used until the pressure difference between two values leading to regime III on the one side and to regime I or II on the other side, is less than 1 Pa. Figure 7 displays this threshold obtained for a shell whose elasticity follows the behavior of a Mooney-Rivlin material with $G = 20$ MPa and $\beta = -1$. An optimum pressure $p^\star$ and its corresponding optimum frequency $f^\star$ can be extracted from numerical simulations for any set of G and β.

B. Frequency dependence

The direct threshold varies differently depending on whether the frequency is higher or lower than the optimum one $f^\star$. In the low frequency regime ($f < f^\star$) the direct

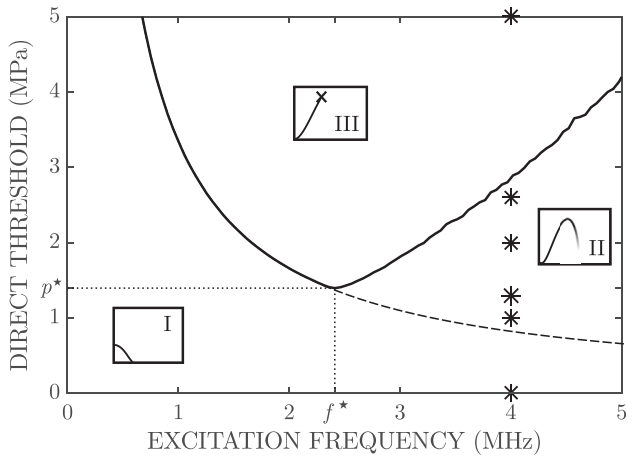

FIG. 7. Acoustic amplitude threshold for the direct vaporization of an encapsulated PFP droplet immersed in water. The shell is a Mooney-Rivlin material with $G = 20$ MPa and $\beta = 1$. The value of the initial droplet size is $a_0 = 1$ μm and the initial bubble radius is $R_0 = 80$ nm. Markers denote the acoustical parameters used for simulations in Fig. 5 ($*$). Small boxes display the three typical regimes for $R(t)$: collapse below dashed line (I), direct vaporization above black line (III), and intermediate behaviors between (II). The frequency $f^\star$ and the pressure $p^\star$ are the optimal acoustic parameters for direct vaporization at a given set of parameters.

threshold is inversely proportional to the frequency and separates regimes I and III. No regime II is observed. This frequency dependence has already been observed for the majority of experimental studies for both micrometric[7,62,63] and nanometric[64,65] particles in the 1–10 MHz range. It is also consistent with the rectified growth threshold p_{gr} of a vapor bubble of PFP in an infinite liquid PFP.[29] This growth threshold ($p_{gr} \propto f^{-1}$) is displayed in Fig. 7 as the lower dashed curve. Rectified growth threshold and direct vaporization threshold are superimposed for $f < f^{\star}$. When the frequency exceeds the optimum ($f > f^{\star}$), the direct threshold starts to increase with frequency. However, below the direct threshold (solid line in Fig. 7) and above the growth threshold (dashed curve in Fig. 7), intermediate solutions of regime II are obtained for the bubble dynamics. This increase in the amount of acoustic energy needed to vaporize the droplet with frequency is reported to our knowledge in at least three experimental studies. In the first one, an increase of vaporization threshold (see Fig. 11 in Ref. 66) is observed between 3 and 4 MHz for quite large droplets in the range 5–27 μm. The authors of this study speculate, however, that the increase of ADV threshold with frequency may be due to the complex geometry of their setup likely enhancing the actual pressure field at the bubble location. In the second one, an increase of the threshold is observed for both nanometric (260 nm) and micrometric (2.2 μm) droplets comparing 1 and 18 MHz excitations (last two lines of Table I in Ref. 67). The third one also notices this trend in the range 1–8 MHz for large particles (5–8 μm mean diameter) but with a large dispersion in their sizes (see Fig. 8 in Ref. 68), though this trend is observed here in a statistical way which may be different from the behavior of a single droplet. These observations are not incompatible with our numerical results as we observe an increase of the threshold with frequency either at very large frequencies as noted by Martin *et al.*,[67] or for large particles as reported by Kripfgans *et al.*[66] and Sheeran *et al.*[68] Moreover, it should be recalled here that vaporization may occur also in regime II (after one or several rebounds, see Fig. 4). Vaporization occurring in this regime is difficult to detect experimentally but may have been recorded at least once: see Fig. 2(D) in Ref. 16, where the radius of a single droplet passes by a maximum, then shrinks to the lowest observable size before finally growing. In our study, when the numerical solution presents at least one rebound event, the solution is disregarded and the amplitude of excitation is increased before solving again the system at the new pressure. Actually, when the acoustic amplitude is relatively close to the growth threshold (dashed curve in Fig. 7), the complete vaporization could appear after at least one rebound and vaporization events exist relatively close to the growth of the initial vapor nucleus (see, for example, excitation at 1.3 MPa in Fig. 5). One can also remark that the direct threshold may be of interest for medical applications; indeed bubble collapse may induce tissue damages and direct vaporization reached in regime III would avoid this.

C. Influence of shell elasticity

The numerical results of Fig. 6 also highlight that the shell rheological properties G and β are significant for the bubble outcome. Therefore, it is interesting to compare the threshold for different rheologies. Figure 8 shows several phase diagrams for a set of parameters (G, β) in order to evaluate the influence of these mechanical parameters. The direct threshold for nonlinear elasticity with $\beta = 1$ is slightly above the one for linear elasticity. When $\beta = -1$, nonlinearities are heightened, the shell is made stiffer for large deformations and the direct threshold increases by about 5 MPa. The second parameter that governs the shell behavior is the shear modulus G. First of all, one observes that the low frequency part of direct threshold does not depend on G and keeps identical to the growth threshold. One can also notice that a bottom limit for the threshold is observed when $G \to 0$ MPa. This shows the vaporization outcome is also controlled by the finite size of the droplet to be evaporated, and not only by the shell elasticity. Indeed, the decrease in the modulus of elasticity results in a reduction of the difference between the direct thresholds for $\beta = 1$ and $\beta = -1$. As soon as G increases, the optimum frequency decreases and the optimum pressure gets higher. Although the optimal point is moved, the low frequency part of the direct threshold curve remains unchanged. Consequently, the shell stiffness should be ideally minimal to ensure the lowest optimum, though a trade-off has to be kept with other effects on *in vivo* performances such as control of dissolution rate. Actually, other numerical simulations (not presented here) show that the relevant parameter that governs the elastic response is indeed the product Gh_0 of the initial shell thickness $h_0 = b_0 - a_0$ times the shear modulus G: varying G or h_0 but keeping the product constant leads to an almost unchanged phase diagram.

D. Influence of geometrical parameters

To understand the high frequency behavior of the direct threshold pressure (when $f > f^{\star}$), another shell characteristics that can be investigated is the particle radius at initial time. The initial shell inner radius a_0 and the initial vapor

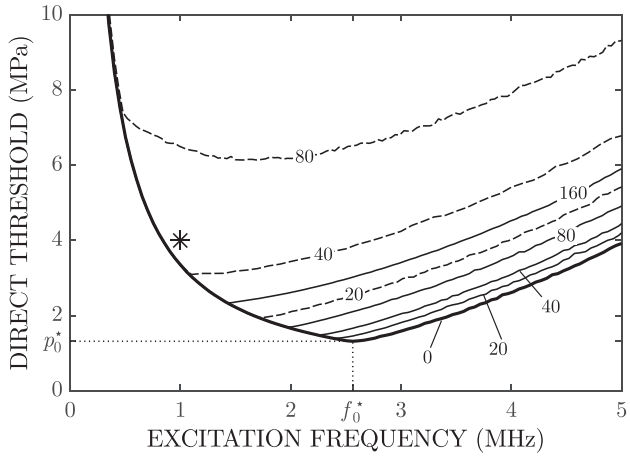

FIG. 8. Direct vaporization threshold as a function of frequency f for different values of shear elasticity G indicated by figures in MPa for $\beta = 1$ (solid lines) and $\beta = -1$ (dashed lines). The marker $(*)$ denotes the acoustical parameters used for simulations in Fig. 6. The geometrical values at initial time are 1 μm and 80 nm, respectively, for the droplet radius a_0 and the bubble radius R_0.

bubble radius R_0 are together linked to the actual quantity of liquid to be vaporized to completely turn the particle content into vapor. Numerical simulations for the direct threshold have thus been computed for three values of a_0 in the cases $R_0 = 40$ nm and $R_0 = 80$ nm as displayed in Fig. 9, for the limit case where elasticity has been removed for the shell ($G \to 0$). The obtained phase diagrams (Fig. 9 top) still exhibit the same low-frequency and high-frequency variations as previous curves: a decreasing phase below the minimal value $p^\star(f^\star)$, followed by an increasing one. For the low frequencies $f < f^\star$, the growth threshold depends mostly on the value of the initial vapor nucleus radius R_0. The influence of the radius a_0 on the low-frequency threshold exists but is negligible in front of the pressure scale precision considered here (1 Pa). This is a very important observation showing that vaporization dynamics at relatively low frequencies is controlled by the nucleus size rather than by the droplet size. The growth threshold therefore amounts from a competition between the time needed for the nucleus to collapse on one side, and on the other side the time of acoustical expansion. As a consequence, even if the nucleus is not centered (as is frequently observed[15,16,26,66] mostly for large micrometric particles), we can expect a very similar behavior because the influence of the encapsulation is weak. So, the effect of nucleus centering will influence the vaporization process mostly for micrometric particles or maybe nanometric ones

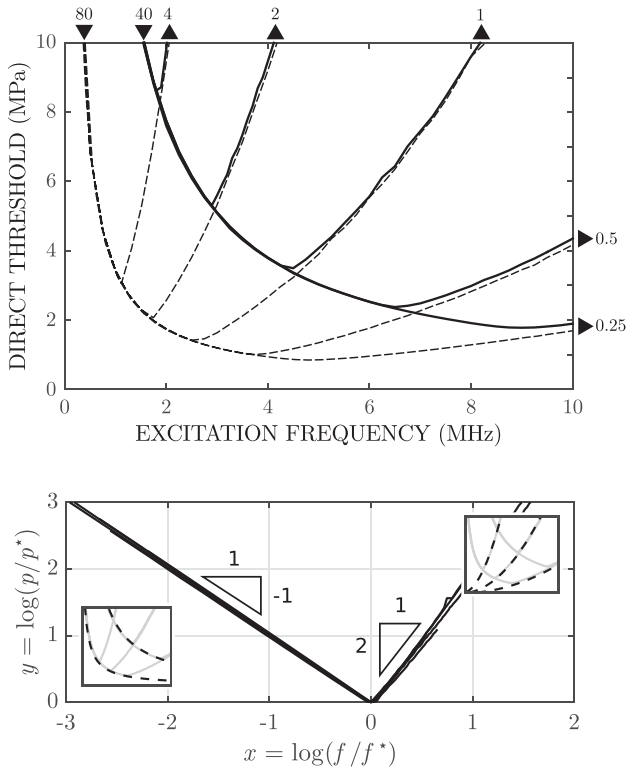

FIG. 9. Top: Direct threshold p_{th} as a function of excitation frequency f for two values of initial vapor radius $R_0 = 40$ (solide line) and 80 nm (dashed line), both computed for five values of initial shell inner radius $a_0 = 0.25$, 0.5, 1, 2, and 4 μm. A curve follows the shortest path from ingoing arrows to outgoing ones. Bottom: log-log representation of the direct threshold normalized by the minimal pressure $p^\star$ as a function of the excitation frequency normalized by the frequency $f^\star$ associated to the minimal pressure.

but only at very high frequencies beyond the optimum point $(p^\star, f^\star)$ (see Fig. 9 top). Consequently, this effect might be of secondary importance for nanodroplets excited at a few MHz (for example, below 5 MHz for 250 nm droplets). Another new feature appearing here in the high frequency domain $f > f^\star$ is the varying slope for the five selected values of a_0. After the turn point $f = f^\star$, the direct threshold slope is significantly dependent on the value of a_0. But whatever the initial bubble radius R_0, this threshold behavior follows the same frequency power law for a given radius a_0. Obviously, when the initial shell inner radius increases, it also means the liquid volume to evaporate is higher and thus more acoustic energy must be supplied. The acoustic pressure required is therefore greater. According to the value imposed on the initial radius a_0, the different curves have strong similarities in their frequency dependence either in the micrometric or nanometric range. If the pressure and the frequency are, respectively, normalized by the optimum pressure and frequency, then the phase diagrams become identical for the whole couples (R_0, a_0) as shown in a log-log representation in Fig. 9 bottom [$y = \log(p_{th}/p^\star)$ versus $x = \log(f/f^\star)$]. Two different dependencies on frequency are observed on both sides of the origin $x = y = 0$. When x is negative, $y = -x$ and the direct threshold is inversely proportional to the frequency. One recovers here the fact that the direct threshold is equal to the growth threshold for $f < f^\star$. On the other hand, positive values approach the law $y = 2x$, highlighting the quadratic frequency dependence.

E. Approximate expression

With these different phase diagrams (Figs. 8 and 9), it is possible to give an approximate analytical expression for the frequency dependence of the direct threshold, valid at least for the particular pressure range]0, 20] MPa. For frequencies $f < f^\star$, the direct threshold, that is almost identical to the rectified growth threshold, is[29]

$$p_{th}(f < f^\star) \simeq A \ln(R^\star/R_0) f^{-1} R_0^{-2}. \tag{24}$$

A is a characteristic constant (unit: kg m s^{-3}) likely linked to the physical properties of the inner liquid (here the PFP). Note that no dependence on the shell properties is observed (see Fig. 8). Indeed, in the low frequency domain, the bubble growth is initiated by rectified heat transfers:[42] the larger the bubble surface is, the more heat conduction can take place and the lower the threshold is. The logarithm dependence $\ln(R^\star/R_0)$ ensures the spontaneous bubble growth for $R_0 < R^\star$. The direct threshold is finally inversely proportional to fR_0^2 as displayed in the left small box in Fig. 9. The dependence in terms of the product fR_0^2 may arise from the competition between applied acoustic expansion and natural condensation. This natural trend to collapse is scaled[69] by the characteristic time

$$t_c \approx \frac{R_0^2}{D} \phi(\mathrm{Ja}), \tag{25}$$

with D the heat diffusion coefficient of the inner liquid and Ja the Jakob number [see for the precise definition Eq. (8) of

Ref. 70 involving the latent heat L and the difference between the temperature of the outer fluid and the boiling temperature of the PFP]. Note that different expressions for the function ϕ are available in the literature.[69] As a consequence, the acoustic excitation has to be sufficiently fast to counterbalance the natural collapse of the bubble during the time t_c, which would explain the fR_0^2 dependence of the direct threshold $p_{\text{th}}(f < f^\star)$.

If the frequency excitation is above $f^\star$ and G approaches zero, the threshold for direct vaporization satisfies the following approximation:

$$p_{\text{th}}(f > f^\star, G = 0) \simeq B_0 f^2 a_0^2, \tag{26}$$

where B_0 is a characteristic constant (unit: kg m^{-3}) likely linked again to the liquid properties. When the initial droplet size decreases, the optimum frequency $f^\star$ shifts to the high frequency. Then, assuming the initial vapor radius to be constant, the minimum pressure required to reach the complete vaporization decreases at a given frequency. However, experimental observations do not show this dependence for nanodroplets.[65,66,68,71,72] This discrepancy is probably linked to the fact that the initial vapor radius is arbitrarily fixed. Actually, this one is very likely dependent on the initial droplet radius, $R_0 = R_0(a_0)$, according to the complex process of homogeneous or inhomogeneous nucleation not investigated here. The increase of the experimentally observed threshold with a decreasing a_0 is therefore compatible with our so-called growth threshold model, provided smaller droplets have a sufficiently smaller vapor nucleus. This seems to be a reasonable assumption. In particular, the coalescence of several nucleation sites for large droplets can generate this situation. This approximated expression is displayed in the right small box in Fig. 9 bottom. By combining Eqs. (24) and (26) both written for the optimum point (denoted by $p_0^\star$ and $f_0^\star$ in Fig. 8), one gets the following approximate expression for this one:

$$\begin{cases} f_0^\star \simeq (AB_0^{-1}\ln(R^\star/R_0)R_0^{-2}a_0^{-2})^{1/3}, \\ p_0^\star \simeq (AB_0^2\ln^2(R^\star/R_0)a_0^2R_0^{-2})^{1/3}. \end{cases} \tag{27}$$

Moreover, Fig. 8 indicates that, at least for the relatively small values of Gh_0 with $\beta = 1$, the pressure for the direct threshold increases linearly with the shear modulus G, independently on frequency. One can therefore assume that

$$p_{\text{th}}(f > f^\star) \simeq B_0 f^2 a_0^2 + CGh_0 + O(G^2 h_0^2), \tag{28}$$

where C is a function expected to depend on the shell initial radius a_0, on its nonlinear elastic coefficient β and on some fluid properties. Plotting $f^\star$ extracted from Fig. 8 versus G for the fixed value $\beta = 1$, one finds a linear dependence of $f^\star$ with elasticity: $f^\star = f_0^\star - \alpha G h_0$ (see Fig. 10 left). Using this approximate law in Eqs. (24) and (28) for the optimum value $f^\star$, equating the two expressions and performing a first order Taylor expansion with respect to G yields $C = 3\alpha B_0 a_0^2 f_0^\star$ and finally leads to

$$p^\star(G) \simeq B_0 a_0^2 (f_0^{\star 2} + \alpha f_0^\star G h_0 + \alpha^2 G^2 h_0^2) \tag{29}$$

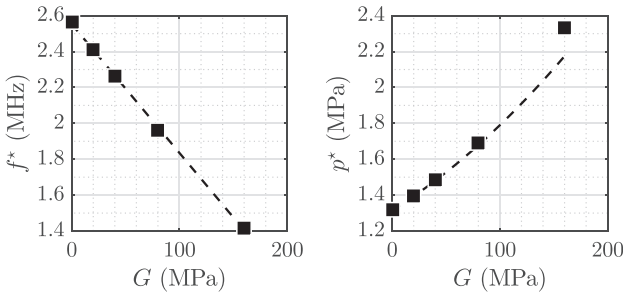

FIG. 10. Left: values (■) for $f^\star$ and linear fit (dashed line) versus shear modulus. Right: values (■) for $p^\star$ and fit [Eq. (29), dashed line] versus shear modulus.

giving the acoustic pressure direct threshold as a function of the thickness and linear elasticity of the shell. This quadratic dependence of the optimum pressure $p^\star$ with G is compared in Fig. 10 (right) with the values of $p^\star$ extracted from Fig. 8 with a very good agreement up to 100 MPa.

VI. CONCLUSION

The acoustic vaporization of an encapsulated droplet has been theoretically and numerically investigated by following the growth of a vapor bubble, already nucleated within a droplet. Particular attention has been given to the influence of the mechanical properties of the encapsulating shell. Given the large changes in volume during the vaporization dynamics, nonlinear elasticity has been taken into account through the strain softening Mooney-Rivlin model describing large but finite deformations of soft materials.

Nonlinearities turn out to have a significant influence on the vaporization process. This one has been classified into three main regimes: collapse (regime I), direct vaporization (regime III), and intermediate behaviors (regime II). The final outcome of the vapor bubble turns out strongly dependent on the shell elastic properties, softest shells with a low value of the shear modulus G and a nonlinear parameter β approaching its maximal value 1, being the most favorable materials for vaporization. However, in the time history of the bubble evolution, the initial phase is mostly a competition between the applied acoustic expansion and the natural collapse of the nucleus: acoustic forcing must be sufficiently fast and strong to counterbalance the collapse. This initial phase is therefore independent on the droplet size and the shell properties, but is strongly influenced by the size of the vapor nucleus. Regarding the threshold necessary to reach direct vaporization (regime III), this explains the observed decreasing low frequency behavior given by Eq. (24) as also reported by several experiments.

This formulation also provides the influence of the initial nucleus size R_0. The dependence on the inner fluid thermal properties is contained in coefficient A and would need further investigations to confirm the role of the characteristic time of condensation. In the high frequency regime, the acoustic excitation is sufficiently fast to allow the bubble to go beyond its critical radius $R^\star$. The bubble now grows naturally but the process needs some time to complete the vaporization of the whole inner liquid. As a consequence, it has to compete with the acoustic excitation which after some time

tends to compress the bubble. This explains the increasing high frequency threshold given by Eq. (26) and proportional to the square of frequency. The high frequency threshold is also given in terms of the initial droplet size and mechanical properties Gh_0 (in the particular case $\beta = 1$). The existence of these two behaviors induces an optimal frequency for which the direct vaporization is achieved at a minimum pressure amplitude. Approximate formulas for these optimum frequency and pressure level have also been provided. Nevertheless, vaporization has also been shown to occur after one or several rebounds, a case which has still to be explored in more details.

That study would deserve many further investigations. From the acoustical point of view, instead of a pure sine wave alternating favorable expansion phases and unfavorable compression phases, the excitation signal could be adapted to minimize the compression phases in order to ease the bubble expansion. The role of nonlinear distortion and superharmonic focusing would also need to be explored. Regarding medical applications, the influence of surrounding tissues, considered as soft elastic solids, would also require attention, especially for targeted drug delivery. For embolotherapy, droplets would be trapped in capillary vessels, which also may modify the droplet growth. This effect is presently not taken into account. Finally, rebounds of the collapsing bubble may be eased by adding dissolved gases. This could be a way to also use regime II in the model with confidence to completely vaporize the inner liquid and to handle a threshold definition with a lower value.

ACKNOWLEDGMENTS

This work is supported by Plan Cancer 2014-2019 (www.plan-cancer.gouv.fr), project AIDA (Acoustically Induced Droplet Vaporization for Anti cancer targeted drug delivery) selected as a research project in Physics, Mathematics, and Engineering Sciences Applied to Cancer Research. T.L. benefits from a Ph.D. scholarship from Université Pierre et Marie Curie (Ecole Doctorale SMAER). Anonymous reviewers are also thanked very much for their numerous and relevant remarks which highly improved the content of the present paper.

APPENDIX A: DETAILS FOR THE CALCULATION OF THE SHELL HYPERELASTIC RESPONSE

The shell elastic reponse $\mathcal{S}$ is associated to the following integral:

$$\mathcal{S} = \int_{\lambda(a)}^{\lambda(b)} \hat{\mathcal{S}}(\lambda)\mathrm{d}\lambda = \int_{\lambda(a)}^{\lambda(b)} \frac{\Psi'(\lambda)}{\lambda^3 - 1}\mathrm{d}\lambda, \tag{A1}$$

where Ψ' is the first derivative of the strain energy function, $\lambda(r) = r/r_0$ is the principal stretch of the deformation, and a and b are, respectively, the inner and the outer radius of the hyperelastic shell. In this work, all the strain energy function considered can be expressed in terms of a linear combination of the principal stretches [see Eq. (13) in Ref. 73] which leads to the formulation of the energy function for an incompressible transformation preserving its spherical symmetry

$$\Psi = \sum_r \mathcal{H}_r \psi(\alpha_r), \tag{A2}$$

where α is a real number, $\mathcal{H}_r$ is the hyperelastic (nonlinear) coefficient, and

$$\psi(\alpha) = \begin{cases} (\lambda^{-2\alpha} + 2\lambda^{\alpha} - 3)/\alpha & (\alpha \neq 0), \\ 0 & (\alpha = 0), \end{cases} \tag{A3}$$

are strain invariants linked to the Mooney-Rivlin invariants such as $I_1 = 2\psi(2)$ and $I_{-1} = -2\psi(-2)$. Because of the nature of the Mooney-Rivlin strain energy, α is restricted to integer values of i and energy becomes

$$\Psi = \sum_i \mathcal{H}_i \psi(2i). \tag{A4}$$

Thus, assuming this form of the energy

$$\hat{\mathcal{S}} = \sum_i \mathcal{H}_i \hat{\mathcal{S}}_i = 2\sum_i \mathcal{H}_i \frac{\lambda^{2i-1} - \lambda^{-4i-1}}{\lambda^3 - 1}, \tag{A5}$$

the shell elastic response satisfies

$$\mathcal{S} = \sum_i \mathcal{H}_i \int_{\lambda(a)}^{\lambda(b)} \hat{\mathcal{S}}_i \mathrm{d}\lambda = \left[\sum_i \mathcal{H}_i \mathcal{S}_i\right]_{\lambda(a)}^{\lambda(b)}. \tag{A6}$$

Two cases must be considered depending on the sign of i before recognizing the sum of the terms of a geometric series valid until $\lambda \neq 1$. For positive values one has

$$\hat{\mathcal{S}}_i = 2\frac{\lambda^{2i}}{\lambda^4}\frac{1 - \lambda^{-6i}}{1 - \lambda^{-3}} = 2\lambda^{2i-4}\sum_{k=0}^{2i-1} \lambda^{-3k}, \tag{A7}$$

whereas for negative ones,

$$\hat{\mathcal{S}}_i = -2\frac{\lambda^{-4i}}{\lambda^4}\frac{1 - \lambda^{6i}}{1 - \lambda^{-3}} = -\frac{2\lambda^{-4i}}{\lambda^4}\sum_{k=0}^{-2i-1} \lambda^{-3k}. \tag{A8}$$

These two cases can be combined in a unique way with the following expression:

$$\hat{\mathcal{S}}_i = 2\,\mathrm{Sgn}(i)\sum_{k=1}^{2|i|} \lambda^{3|i|-i-1-3k}, \tag{A9}$$

where the function $\mathrm{Sgn}(x)$ is introduced that returns the sign of x. This expression remains valid for all integer values of $i \neq 0$. It can be finally integrated to give the general elastic response of the shell,

$$\mathcal{S}_i = 2\,\mathrm{Sgn}(i)\sum_{k=1}^{2|i|} \frac{\lambda^{3|i|-i-3k}}{3|i| - i - 3k}. \tag{A10}$$

Relation (A10) holds for $i \neq 3p$ ($p \in \mathbb{Z}^*$), otherwise

$$\mathcal{S}_i = 2\,\mathrm{Sgn}(p)\left[\ln(\lambda) + \sum_{q=0}^{1}\sum_{k=1}^{M}\frac{\lambda^{3k(2q-1)}}{3k(2q-1)}\right], \tag{A11}$$

with $M = 3|p| + (1-2q)p - q$. When Eq. (A10) is applied to the Mooney-Rivlin material for which

$$\mathcal{H}_i = \frac{G(1+i\beta)}{2i} \quad \text{and} \quad i = \{-1, 1\}, \tag{A12}$$

then $|i| = 1$ and $\mathrm{Sgn}(i)/i = |1|^{-1} = 1$, and the following elastic response is obtained:

$$\mathcal{S} = \left[\sum_{i=-1}^{1}\sum_{k=0}^{1}\frac{G(1+i\beta)}{-i-3k}\lambda^{-i-3k}\right]_{\lambda(a)}^{\lambda(b)}, \tag{A13}$$

or in its expanded form

$$\mathcal{S}/G = (1+\beta)\left(\frac{a_0}{a} - \frac{b_0}{b} + \frac{a_0^4}{4a^4} - \frac{b_0^4}{4b^4}\right), \\ +(1-\beta)\left(\frac{b}{b_0} - \frac{a}{a_0} - \frac{b_0^2}{2b^2} + \frac{a_0^2}{2a^2}\right). \tag{A14}$$

When assuming an infinite elastic medium with Mooney-Rivlin elasticity outside the droplet ($b_0 \to \infty$), this result is consistent with the result of Gaudron *et al.*[74] given by Eq. (A4) for $1+\beta = -2\eta$ and $1-\beta = 2\eta$.

APPENDIX B: REMARK ON ACOUSTIC EXCITATION

In the present study, an acoustic forcing of the form $p_a(t) = -P\sin\omega t$ has been chosen, assuming the vapor nucleus is already nucleated at initial time. However, most studies indicate that initial nucleation occurs near the peak of the negative half-cycle rather than at the beginning of it as a result of the initial energy barrier to homogeneous nucleation.

In a recent study, Miles *et al.*[27] compared experimental results of ADV threshold with the classical homogeneous nucleation theory for micrometric particles (from 3 to 30 μm) excited at 7.5 MHz taking into account both the nonlinear distortion of the pressure field and the droplet scattering. They duly pointed out that the quasi-static nucleation theory would need to be completed by a dynamical bubble growth model such as the present one. To match the expectation that homogeneous nucleation occurs not at initial time but most likely around the peak negative pressure, they suggested a driving pressure of the form $p_a(t) = -P\cos\omega t$ ($t > 0$). We have tried such simulations with a cosine excitation instead of a sine one with other initial conditions unchanged. The discontinuity in the driving pressure induces indeed a high frequency excitation. As a consequence, all of our observed low frequency behaviors are discarded and we observe only an increasing direct threshold with frequency. As this is not consistent with most of the experimental observations, it is likely that the full mechanism is more complex to model and would require coupling the present model of bubble dynamics with one of nucleation.

Another study[25] provides quantitative data about the phase of the "nucleation moment" relative to the acoustic excitation. By recording the *droplet radius* versus time using high speed imaging and deducing from it the actual pressure excitation thanks to the Rayleigh-Plesset equation, the so-called "nucleation moment" could be estimated. Note this moment is indeed rather the moment at which the bubble growth begins to inflate the droplet. The present model allows us to simulate this "nucleation moment" and to compare it with those previous experimental observations. This is presented in the two insets of Fig. 11, where the bubble radius $R(t)$ and the droplet inner radius $a(t)$ are plotted as a function of time for three different cases: (a) $f = 1$ MHz, $P = 4$ MPa, and $a_0 = 1$ μm [$R(t)$ was already shown in Fig. 6], (b) $f = 4$ MHz, $P = 5$ MPa, and $a_0 = 1$ μm [$R(t)$ was already shown in Fig. 5], and (c) $f = 3.5$ MHz, $P = 4.5$ MPa, and $a_0 = 5$ μm (corresponding to the experimental conditions of Ref. 25). In all cases, the shell parameters are $G = 20$ MPa and $\beta = 1$ so as to keep a weak influence of the encapsulation, and $R_0 = R^\star/8 \approx 80$ nm.

The two first cases lead to a direct droplet vaporization (regime III). The bubble first grows without disturbing the droplet, and this one inflates only when the bubble size has almost reached its initial size. Then, there remains very little liquid to vaporize, the droplet begins to grow following very closely the bubble growth until the remaining tiny liquid film completely evaporates. The last case (c) leads to a final collapse after the droplet has undergone three oscillations (regime II). The early dynamics of the process is quite similar (though much more visible because of the larger droplet size). However, because there remains much more liquid to vaporize than in cases (a) and (b), the complete vaporization cannot be achieved here before acoustic recompression inhibits the ADV process. Note that in the experiment,[25] the acoustic excitation was turned off after a few cycles thus

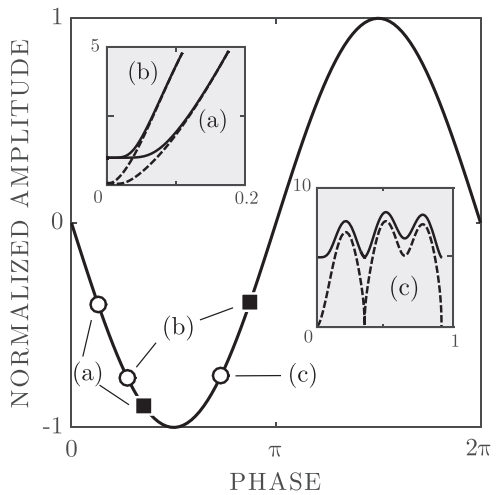

FIG. 11. Time of the "nucleation moment" (◯) and time of complete vaporization (■) superimposed to the acoustic excitation (solid line) in dimensionless variable ωt and normalized amplitude for three different cases: (a) $a_0 = 1$ μm, $f = 1$ MHz, and $P = 4$ MPa, (b) $a_0 = 1$ μm, $f = 4$ MHz, and $P = 5$ MPa, and (c) $a_0 = 5$ μm, $f = 3.5$ MHz, and $P = 4.5$ MPa. Insets: corresponding bubble radius (dashed lines) and droplet radius (solid lines) in micrometer versus time in ms.

allowing a growth of the droplet. The figure superimposes to the acoustic excitation in dimensionless variable ωt, (i) the vaporization moments for cases (a) and (b) (denoted as black squares) and (ii) the moment at which the droplet begins to inflate, which is defined arbitrarily as the first time at which $a(t) > 1.1a_0$ (denoted as white circles). This last event is to be compared to the "nucleation moment" estimated in Fig. 6 in Ref. 25. For the cases (a) and (b), this event occurs before the peak negative pressure. Increasing the frequency tends however to delay this event closer to the negative peak. The time of complete vaporization occurs of course later, either before [case (a)] or after [case (b)] the negative peak. For larger droplets [case (c)], the nucleation moment occurs after the peak, in qualitative agreement with experimental observations.[25] These simulations also indicate a significant sensitivity of the phase shift between acoustic and droplet response with geometrical and acoustical parameters. This issue would require a deeper investigation and more comparisons with experiments.

[1]C.-Y. Lin and W. G. Pitt, "Acoustic droplet vaporization in biology and medicine," BioMed Res. Int. **2013**, 404361 (2013).
[2]H. Hashizume, P. Baluk, S. Morikawa, J. W. McLean, G. Thurston, S. Roberge, R. K. Jain, and D. M. McDonald, "Openings between defective endothelial cells explain tumor vessel leakiness," Am. J. Pathol. **156**, 1363–1380 (2000).
[3]A. K. Iyer, G. Khaled, J. Fang, and H. Maeda, "Exploiting the enhanced permeability and retention effect for tumor targeting," Drug Discov. Today **11**, 812–818 (2006).
[4]D. Pan, G. M. Lanza, S. A. Wickline, and S. D. Caruthers, "Nanomedicine: Perspective and promises with ligand-directed molecular imaging," Eur. J. Radiol. **70**, 274–285 (2009).
[5]N. Bertrand, J. Wu, X. Xu, N. Kamaly, and O. C. Farokhzad, "Cancer nanotechnology: The impact of passive and active targeting in the era of modern cancer biology," Adv. Drug Deliv. Rev. **66**, 2–25 (2014).
[6]M. N. Khalid, P. Simard, D. Hoarau, A. Dragomir, and J.-C. Leroux, "Long circulating poly (ethylene glycol)-decorated lipid nanocapsules deliver docetaxel to solid tumors," Pharm. Res. **23**, 752–758 (2006).
[7]O. D. Kripfgans, J. B. Fowlkes, D. L. Miller, O. P. Eldevik, and P. L. Carson, "Acoustic droplet vaporization for therapeutic and diagnostic applications," Ultrasound Med. Biol. **26**, 1177–1189 (2000).
[8]D. Cosco, E. Fattal, M. Fresta, and N. Tsapis, "Perfluorocarbon-loaded micro and nanosystems for medical imaging: A state of the art," J. Fluorine Chem. **171**, 18–26 (2015).
[9]M. Zhang, M. L. Fabiilli, K. J. Haworth, J. B. Fowlkes, O. D. Kripfgans, W. Roberts, K. Ives, and P. L. Carson, "Initial investigation of acoustic droplet vaporization for occlusion in canine kidney," Ultrasound Med. Biol. **36**, 1691–1703 (2010).
[10]P. S. Sheeran, S. H. Luois, L. B. Mullin, T. O. Matsunaga, and P. A. Dayton, "Design of ultrasonically-activatable nanoparticles using low boiling point perfluorocarbons," Biomaterials **33**, 3262–3269 (2012).
[11]N. Rapoport, "Phase-shift, stimuli-responsive perfluorocarbon nanodroplets for drug delivery to cancer," Wiley Interdiscip. Rev. Nanomed. Nanobiotechnol. **4**, 492–510 (2012).
[12]E. Pisani, N. Tsapis, B. Galaz, M. Santin, R. Berti, N. Taulier, E. Kurtisovski, O. Lucidarme, M. Ourevitch, B. T. Doan, J. C. Beloeil, B. Gillet, W. Urbach, S. L. Bridal, and E. Fattal, "Perfluorooctyl bromide polymeric capsules as dual contrast agents for ultrasonography and magnetic resonance imaging," Adv. Funct. Mater. **18**, 2963–2971 (2008).
[13]A. A. Doinikov, P. S. Sheeran, A. Bouakaz, and P. A. Dayton, "Vaporization dynamics of volatile perfluorocarbon droplets: A theoretical model and *in vitro* validation," Med. Phys. **41**, 102901 (2014).
[14]K. Astafyeva, J.-L. Thomas, F. Coulouvrat, M. Guédra, O. Diou, L. Mousnier, N. Tsapis, W. Urbach, and N. Taulier, "Properties of theranostic nanoparticles determined in suspension by ultrasonic spectroscopy," Phys. Chem. Chem. Phys. **17**, 25483–25493 (2015).
[15]D. S. Li, O. D. Kripfgans, M. L. Fabiilli, J. Brian Fowlkes, and J. L. Bull, "Initial nucleation site formation due to acoustic droplet vaporization," Appl. Phys. Lett. **104**, 063703 (2014).
[16]O. Shpak, L. Stricker, M. Versluis, and D. Lohse, "The role of gas in ultrasonically driven vapor bubble growth," Phys. Med. Biol. **58**, 2523–2535 (2013).
[17]D. S. Li, O. D. Kripfgans, M. L. Fabiilli, J. Brian Fowlkes, and J. L. Bull, "Formation of toroidal bubbles from acoustic droplet vaporization," Appl. Phys. Lett. **104**, 063706 (2014).
[18]W. H. Besant, *A Treatise on Hydrostatics and Hydrodynamics* (Deighton, Bell, Cambridge, 1859).
[19]L. Rayleigh, "On the pressure developed in a liquid during the collapse of a spherical cavity," Lond. Edinb. Dubl. Philos. Mag. **34**, 94–98 (1917).
[20]M. S. Plesset and S. A. Zwick, "The growth of vapor bubbles in superheated liquids," J. Appl. Phys. **25**, 493–500 (1954).
[21]B. E. Noltingk and E. A. Neppiras, "Cavitation produced by ultrasonics," Proc. Phys. Soc. London, Sect. B **63**, 674–685 (1950).
[22]Y. Yasui, "Variation of liquid temperature at bubble wall near the sonoluminescence threshold," J. Phys. Soc. Jpn. **65**, 2830–2840 (1996).
[23]J. B. Keller and I. I. Kolodner, "Damping of underwater explosion bubble oscillations," J. Appl. Phys. **27**, 1152–1161 (1956).
[24]N. A. Gumerov, "Dynamics of vapor bubbles with nonequilibrium phase transitions in isotropic acoustic fields," Phys. Fluids **12**, 71–88 (2000).
[25]O. Shpak, T. J. Kokhuis, Y. Luan, D. Lohse, N. de Jong, B. Fowlkes, M. Fabiilli, and M. Versluis, "Ultrafast dynamics of the acoustic vaporization of phase-change microdroplets," J. Acoust. Soc. Am. **134**, 1610–1621 (2013).
[26]O. Shpak, M. Verweij, H. J. Vos, N. de Jong, D. Lohse, and M. Versluis, "Acoustic droplet vaporization is initiated by superharmonic focusing," Proc. Natl. Acad. Sci. U.S.A. **111**, 1697–1702 (2014).
[27]C. J. Miles, C. R. Doering, and O. D. Kripfgans, "Nucleation pressure threshold in acoustic droplet vaporization," J. Appl. Phys. **120**, 034903 (2016).
[28]Y. Hao and A. Prosperetti, "The dynamics of vapor bubbles in acoustic pressure fields," Phys. Fluids **11**, 2008–2019 (1999).
[29]M. Guédra and F. Coulouvrat, "A model for acoustic vaporization of encapsulated droplets," J. Acoust. Soc. Am. **138**, 3656–3667 (2015).
[30]C. C. Church, "The effects of an elastic solid surface layer on the radial pulsations of gas bubbles," J. Acoust. Soc. Am. **97**, 1510–1521 (1995).
[31]Z. Z. Wong, O. D. Kripfgans, A. Qamar, J. B. Fowlkes, and J. L. Bull, "Bubble evolution in acoustic droplet vaporization at physiological temperature via ultra-high speed imaging," Soft Matter **7**, 4009–4016 (2011).
[32]A. A. Doinikov and P. A. Dayton, "Maxwell rheological model for lipid-shelled ultrasound microbubble contrast agents," J. Acoust. Soc. Am. **121**, 3331–3340 (2007).
[33]K. Tsiglifis and N. A. Pelekasis, "Nonlinear radial oscillations of encapsulated microbubbles subject to ultrasound: The effect of membrane constitutive law," J. Acoust. Soc. Am. **123**, 4059–4070 (2008).
[34]S. Paul, A. Katiyar, K. Sarkar, D. Chatterjee, W. T. Shi, and F. Forsberg, "Material characterization of the encapsulation of an ultrasound contrast microbubble and its subharmonic response: Strain-softening interfacial elasticity model," J. Acoust. Soc. Am. **127**, 3846–3857 (2010).
[35]M. Mooney, "A theory of large elastic deformation," J. Appl. Phys. **11**, 582–592 (1940).
[36]R. S. Rivlin and D. W. Saunders, "Large elastic deformations of isotropic materials. VII. Experiments on the deformation of rubber," Philos. Trans. A: Math. Phys. Eng. Sci. **243**, 251–288 (1951).
[37]M. Guédra, T. Valier-Brasier, J.-M. Conoir, F. Coulouvrat, K. Astafyeva, and J.-L. Thomas, "Influence of shell compressibility on the ultrasonic properties of polydispersed suspensions of nanometric encapsulated droplets," J. Acoust. Soc. Am. **135**, 1044–1055 (2014).
[38]K. Radhakrishnan, C. K. Holland, and K. J. Haworth, "Scavenging dissolved oxygen via acoustic droplet vaporization," Ultrason. Sonochem. **31**, 394–403 (2016).
[39]R. D. Finch and E. A. Neppiras, "Vapor bubble dynamics," J. Acoust. Soc. Am. **53**, 1402–1410 (1973).
[40]C. E. Brennen, *Cavitation and Bubble Dynamics* (Cambridge University Press, New York, 2014).
[41]A. Prosperetti, "Boundary conditions at a liquid-vapor interface," Meccanica **14**, 34–47 (1979).
[42]A. Prosperetti and M. S. Plesset, "Vapour-bubble growth in a superheated liquid," J. Fluid Mech. **85**, 349–368 (1978).
[43]R. Ogden and Y. B. Fu, *Nonlinear Elasticity: Theory and Applications* (Cambridge University Press, New York, 2001).
[44]N. Reznik, M. Seo, R. Williams, E. Bolewska-Pedyczak, M. Lee, N. Matsuura, J. Gariepy, F. S. Foster, and P. N. Burns, "Optical studies of vaporization and stability of fluorescently labelled perfluorocarbon droplets," Phys. Med. Biol. **57**, 7205–7217 (2012).

[45]R. W. Ogden, "Incremental statics and dynamics of pre-stressed elastic materials," in *Waves in Nonlinear Pre-Stressed Materials* (Springer Vienna, Vienna, 2007), pp. 1–26.
[46]R. Mangan and M. Destrade, "Gent models for the inflation of spherical balloons," Int. J. Non-Linear Mech. **68**, 52–58 (2015).
[47]R. W. Ogden, "On isotropic tensors and elastic moduli," Math. Proc. Cambridge Philos. Soc. **75**, 427–436 (1974).
[48]L. D. Landau and E. M. Lifshitz, *Course of Theoretical Physics Vol 7: Theory and Elasticity* (Pergamon, New York, 1959).
[49]D. M. Egle and D. E. Bray, "Measurement of acoustoelastic and third-order elastic constants for rail steel," J. Acoust. Soc. Am. **60**, 741–744 (1976).
[50]S. Kostek, B. K. Sinha, and A. N. Norris, "Third-order elastic constants for an inviscid fluid," J. Acoust. Soc. Am. **94**, 3014–3017 (1993).
[51]J.-L. Gennisson, M. Rénier, S. Catheline, C. Barriére, J. Bercoff, M. Tanter, and M. Fink, "Acoustoelasticity in soft solids: Assessment of the nonlinear shear modulus with the acoustic radiation force," J. Acoust. Soc. Am. **122**, 3211–3219 (2007).
[52]M. F. Hamilton, Y. A. Ilinskii, and E. A. Zabolotskaya, "Separation of compressibility and shear deformation in the elastic energy density (L)," J. Acoust. Soc. Am. **116**, 41–44 (2004).
[53]S. Y. Emelianov, M. F. Hamilton, Y. A. Ilinskii, and E. A. Zabolotskaya, "Nonlinear dynamics of a gas bubble in an incompressible elastic medium," J. Acoust. Soc. Am. **115**, 581–588 (2004).
[54]E. A. Kearsley, "Note: Strain invariants expressed as average stretches," J. Rheol. **33**, 757–760 (1989).
[55]L. R. G. Treloar, "The structure and elasticity of rubber," Rep. Prog. Phys. **9**, 113–136 (1942).
[56]http://fluoromed.com/ (Last viewed 4/6/2017).
[57]P. Marmottant, S. van der Meer, M. Emmer, M. Versluis, N. de Jong, S. Hilgenfeldt, and D. Lohse, "A model for large amplitude oscillations of coated bubbles accounting for buckling and rupture," J. Acoust. Soc. Am. **118**, 3499–3505 (2005).
[58]A. S. Hannah, G. P. Luke, and S. Y. Emelianov, "Blinking phase-change nanocapsules enable background-free ultrasound imaging," Theranostics **6**, 1866–1876 (2016).
[59]H. Yoon, S. K. Yarmoska, A. S. Hannah, C. Yoon, K. A. Hallam, and S. Y. Emelianov, "Contrast-enhanced ultrasound imaging *in vivo* with laser-activated nanodroplets," Med. Phys. **44**, 3444–3449 (2017).
[60]C. C. Church, "Spontaneous homogeneous nucleation, inertial cavitation and the safety of diagnostic ultrasound," Ultrasound Med. Biol. **28**, 1349–1364 (2002).
[61]P. A. Mountford and M. A. Borden, "On the thermodynamics and kinetics of superheated fluorocarbon phase-change agents," Adv. Colloid Interface Sci. **237**, 15–27 (2016).
[62]O. D. Kripfgans, J. B. Fowlkes, M. Woydt, O. P. Eldevik, and P. L. Carson, "*In vivo* droplet vaporization for occlusion therapy and phase aberration correction," IEEE Trans. Ultrasonics Ferroelectr. Freq. Control **49**, 726–738 (2002).
[63]K. C. Schad and K. Hynynen, "*In vitro* characterization of perfluorocarbon droplets for focused ultrasound therapy," Phys. Med. Biol. **55**, 4933–4947 (2010).
[64]R. Williams, C. Wright, E. Cherin, N. Reznik, M. Lee, I. Gorelikov, F. S. Foster, N. Matsuura, and P. N. Burns, "Characterization of submicron phase-change perfluorocarbon droplets for extravascular ultrasound imaging of cancer," Ultrasound Med. Biol. **39**, 475–489 (2013).
[65]P. S. Sheeran, V. P. Wong, S. Luois, R. J. McFarland, W. D. Ross, S. Feingold, T. O. Matsunaga, and P. A. Dayton, "Decafluorobutane as a phase-change contrast agent for low-energy extravascular ultrasonic imaging," Ultrasound Med. Biol. **37**, 1518–1530 (2011).
[66]O. D. Kripfgans, M. L. Fabiilli, P. L. Carson, and J. B. Fowlkes, "On the acoustic vaporization of micrometer-sized droplets," J. Acoust. Soc. Am. **116**, 272–281 (2004).
[67]A. L. Martin, M. Seo, R. Williams, G. Belayneh, F. S. Foster, and N. Matsuura, "Intracellular growth of nanoscale perfluorocarbon droplets for enhanced ultrasound-induced phase-change conversion," Ultrasound Med. Biol. **38**, 1799–1810 (2012).
[68]P. S. Sheeran, T. O. Matsunaga, and P. A. Dayton, "Phase-transition thresholds and vaporization phenomena for ultrasound phase-change nanoemulsions assessed via high-speed optical microscopy," Phys. Med. Biol. **58**, 4513–4534 (2013).
[69]A. Prosperetti, "Vapor bubbles," Annu. Rev. Fluid Mech. **49**, 221–248 (2017).
[70]Y. Hao and A. Prosperetti, "Rectified heat transfer into translating and pulsating vapor bubbles," J. Acoust. Soc. Am. **112**, 1787–1796 (2002).
[71]M. L. Fabiilli, K. J. Haworth, N. H. Fakhri, O. D. Kripfgans, P. L. Carson, and J. B. Fowlkes, "The role of inertial cavitation in acoustic droplet vaporization," IEEE Trans. Ultrasonics Ferroelectr. Freq. Control **56**, 1006–1017 (2009).
[72]M. L. Fabiilli, K. J. Haworth, I. E. Sebastian, O. D. Kripfgans, P. L. Carson, and J. B. Fowlkes, "Delivery of chlorambucil using an acoustically-triggered perfluoropentane emulsion," Ultrasound Med. Biol. **36**, 1364–1375 (2010).
[73]R. Ogden, "Large deformation isotropic elasticity—On the correlation of theory and experiment for incompressible rubberlike solids," R. Soc. **326**, 565–584 (1972).
[74]R. Gaudron, M. T. Warnez, and E. Johnsen, "Bubble dynamics in a viscoelastic medium with nonlinear elasticity," J. Fluid Mech. **766**, 54–75 (2015).